

AIAA

DELAMINATION AND STITCHED FAILURE IN
STITCHED COMPOSITE JOINTS

E. H. Glaessgen, I. S. Raju, and C. C. Poe, Jr.
NASA Langley Research Center
Hampton, Virginia

AIAA Paper No. 99-1247

Presented at the
40th AIAA/ASME/ASCE/AHS/ASC
Structures, Structural Dynamics,
and Materials Conference and Exhibit
St. Louis, Missouri
April 12-15, 1999

DELAMINATION AND STITCH FAILURE IN STITCHED COMPOSITE JOINTS

E.H. Glaessgen,^{*} I.S. Raju[†] and C.C. Poe, Jr.[‡]
NASA Langley Research Center, Hampton, VA 23681-0001, U.S.A.

Abstract

The effect of stitches on the failure of a single lap joint configuration was determined in a combined experimental and finite element study. The experimental program was conducted to determine debond growth under static monotonic loading. The stitches were shown to delay the initiation of the debond and provide load transfer beyond the load necessary to completely debond the stitched lap joint. The experimentally determined debond length vs. applied load was used as an input parameter in the finite element analysis of both configurations. The strain energy release rates at the debond front were calculated using plate finite elements. Nonlinear fastener elements were used to model the stitches and multipoint constraints were used to model the contact problem. Models of the unstitched configuration showed significant values of modes I and II across the width of the joint and showed that mode III is zero at the centerline but increases near the free edge. Models of the stitched configuration showed that the stitches were effective in reducing mode I to zero, but had less of an effect on modes II and III.

Introduction

Stitched warp-knit textile composite materials are currently being considered for use in primary aerospace structures. Structures manufactured from these materials offer advantages in manufacturability and damage tolerance over conventional composite and metallic structures. Manufacturability is improved because large sections of dry carbon textile preform can be assembled and stitched with Kevlar threads near net shape before the epoxy resin is introduced.¹ Improvements in damage tolerance are observed because the Kevlar stitches tend to prevent propagation of debonds and delaminations that may be caused by in-plane and out-of-plane loadings.²

Often it is impossible to manufacture a complete component as a continuous structure, and hence separate sections of the component need to be joined together. This is often achieved through the use of bonded or bolted joints. The analysis of bonded and bolted joints has received considerable attention over the past three decades.³⁻¹² Standard practice guidelines for the analysis of bonded and bolted joints have been documented in reference.¹³ Rather than bolting or bonding sections, the method for joining sections of warp-knit textile composites that is discussed in this paper involves the use of stitching. The potential benefits of stitching joints are similar to those for stitching any other textile composite structure and include improved manufacturability, increased static strength and increased damage tolerance.^{1,2,14}

Figure 1 shows a cylindrical composite structure where a stitched lap joint is used to join two sections. Figure 1(b) shows the region near the stitched lap joint in a cylindrical section where debonding may occur while Figure 1(c) shows a simplified rectangular configuration that may be used to gain insight into the behavior of the more complex configurations.

This objective of this paper is to quantify the effect of stitches on the response of lap joints in warp knit carbon epoxy textile composites under monotonic tensile loading. Failure mechanisms and failure loads of unstitched and stitched lap joints will be determined using a combined analytical and experimental technique. Comparison will be made between the experimentally determined failure loads of the stitched and similar unstitched lap joint panels to assess the contribution of the stitches to preventing delamination growth. Strain energy release rates and stitch forces will be evaluated using finite element analyses implementing the experimentally determined load vs. crack length.

Lap Joint Configuration

A stitched lap joint subjected to remote tensile loading is shown in Figure 1(c) and configurational details of the deformed configuration are shown in Figure 2. The configurational parameters of this joint are the length of the composite, L_1 , the length of the overlap, L_2 , the width of the coupon, b , and the thickness of the coupon, t . The local details of a debond of length, a ,

* Research Associate, National Research Council

† Head, Mechanics of Materials Branch, Associate Fellow AIAA

‡ Senior Scientist, Mechanics of Materials Branch

Copyright 1999 by the American Institute of Aeronautics and Astronautics, Inc. No copyright is asserted in the United States under Title 17, U.S. Code. The U.S. Government has a royalty-free license to exercise all rights under the copyright claimed herein for Governmental Purposes. All other rights are reserved by the copyright owner.

propagating from the end of the lap joint including the loading of the stitches are shown in the figure.

Material and skin thicknesses that are representative of the hybrid IM7/3501-6 and AS4/3501-6 warp-knit fabric stitched composite upper wing skin used in the NASA Advanced Subsonic Technology (AST) program are considered.¹ The material consists of IM7 yarns in the axial direction and AS4 yarns in the off-axis directions. Each stack of material is assumed to be oriented with its primary axis in the x -direction and having a thickness of 0.055 in. The overall density of the fabric expressed in areal weight is 0.577 oz./ft.², 1.21 oz./ft.² and 0.651 oz./ft.² for the forty-five, zero and ninety degree plies, respectively. The equivalent laminate stacking sequence of each stack of material is (45/-45/0/90/0/-45/45)_n where $n=2$ for both of the joined laminates. This stacking sequence will become important in the discussion of the debond growth that follows in the section on experimental results.

A lap joint panel was made with half of its surface unstitched and half of its surface stitched. Specimens were machined from the unstitched and stitched portion of the panel to the dimensions given in Table 1. The specimens were loaded in monotonic tension at a rate of 0.05 in./min. The debonds initiated and grew at the ends of the lap joints. The failure loads for coupons with and without stitching were determined. The increase in debond length with increasing load was determined using a radiographic technique.

Finite Element Analysis

Figure 1 shows a cylindrical composite shell with a lap joint. Three-dimensional modeling and analysis of this complex configuration may require a large finite element model with several hundred thousand degrees of freedom. However, considerable insight into the behavior of such a complicated configuration can be obtained by studying simpler configurations such as the strip lap joint configuration shown in Figure 2 while reducing modeling complexity. The strip lap joint configuration was modeled using the STAGS finite element code.^{15,16}

In the literature, models based on quasi-3D or 3D brick finite element models have been used to study edge delamination and near-surface delamination of composites.¹⁷⁻¹⁹ Since many layers of brick elements are often required to model the configurations, finite element

models with large numbers of degrees-of-freedom may be required. References 20-24 proposed the use of plate elements in conjunction with the virtual crack closure technique (VCCT) to model skin-stiffener debond problems. The plate element models were used to evaluate accurate values of mode I and mode II strain energy release rates.

The plate element-based finite element models have been extended to determine strain energy release rates in stitched skin-stiffener configurations.^{25,26} Similar techniques may be used to determine strain energy release rates for the stitched lap joint configuration shown in Figure 1(c). The method of analysis involves the use of plate elements to model the configuration, nonlinear fastener elements to model the stitches and multipoint constraints to model the contact problem. Since the nodes of the plate elements modeling the two laps are coincident, finite length spar or beam elements cannot be used to model the stitches as in references.²⁷⁻³⁴ Rather, the stitches are modeled as nonlinear fastener elements with experimentally determined axial and shear compliances. These compliances were determined using independent flatwise tension and double lap shear tests. On these figures, the nonlinear fastener elements are schematically shown as springs. This modeling technique allows an experimentally determined load vs. deflection behavior to be considered for each stitch and includes the local effects of the stitch debonding from the laminate in addition to nonlinearity of the stitch material itself.³⁵

The specimen configurational parameters, stitch column spacing and stitch row spacing are shown in Figure 2 and Table 1. Debond lengths, a , between 0.250 in. and 1.50 in. are considered for the unstitched and stitched configurations.

Material Properties

In these analyses, the laminates are assumed to be homogeneous with axial properties determined experimentally and all others estimated using the equivalent stacking sequence and classical lamination theory as

$$\begin{aligned} E_{11} &= 11.7 \text{ Ms}i & \mu_{12} &= 2.50 \text{ Ms}i & \nu_{12} &= 0.40 \\ E_{22} &= 5.14 \text{ Ms}i & \mu_{13} &= 1.77 \text{ Ms}i & \nu_{13} &= 0.30 \\ E_{33} &= 1.79 \text{ Ms}i & \mu_{23} &= 0.88 \text{ Ms}i & \nu_{23} &= 0.30 \end{aligned}$$

where E_{ij} , μ_{ij} , ν_{ij} ($i,j=1,2,3$) are the Young's moduli, shear moduli, and Poisson's ratio, respectively, and the

Table 1: Test Specimen Dimensions

Panel	Stitch Column Spacing, S_x , in.	Stitch Row Spacing, S_y , in.	Thickness, t , in.	Width, b , in.	Lap length, L_2 , in.	Length, L_1 , in.
1	0.125	0.125	0.110	1.00	3.69	27.0

subscripts 1,2,3 represent the fiber, transverse and out-of-plane directions, respectively.

Strain Energy Release Rates

The configuration was modeled with the STAGS (Structural Analysis of General Shells) finite element code using a 9-node quadratic shear deformable plate/shell element.^{15,16} The virtual crack closure technique (VCCT)^{36,37} was used to calculate strain energy release rates, G , with plate elements using the techniques discussed in references 20-24. A comparison of strain energy release rates computed with the plate element-based models and similar plane strain element-based models for skin-stiffener configurations without stitching is discussed in reference 26. Additional considerations that arise from debond modeling with plate elements are discussed in reference 24.

A representation of the 9-noded plate elements near a debond front with rectangular grid type modeling is shown in Figure 3 with elements having both length and width of 0.0625 in. Reference 24 suggests that allowing the elements ahead of the debond front to have free rotations ensures accurate modeling and evaluation of the strain energy release rates. If there are free rotations ahead of the debond front, then the G values can be calculated using the nodal forces (F_x , F_y , F_z) and displacements (u , v , w) near the debond front and the increment of new debond area created as (see Figure 3)²⁰

Mode-I components:

$$(G_I)_i = -\frac{1}{2\Delta b_i} [F_{z_i}(w_p - w_{p'}) + F_{z_e}(w_l - w_r)] \\ (G_I)_j = -\frac{1}{2\Delta b_j} [F_{z_j}(w_q - w_{q'}) + F_{z_f}(w_m - w_{m'})] \quad (1) \\ (G_I)_k = -\frac{1}{2\Delta b_k} [F_{z_k}(w_r - w_{r'}) + F_{z_s}(w_n - w_{n'})]$$

Mode-II components:

$$(G_{II})_i = -\frac{1}{2\Delta b_i} [F_{x_i}(u_p - u_{p'}) + F_{x_e}(u_l - u_r)] \\ (G_{II})_j = -\frac{1}{2\Delta b_j} [F_{x_j}(u_q - u_{q'}) + F_{x_f}(u_m - u_{m'})] \quad (2) \\ (G_{II})_k = -\frac{1}{2\Delta b_k} [F_{x_k}(u_r - u_{r'}) + F_{x_s}(u_n - u_{n'})]$$

Mode-III components:

$$(G_{III})_i = -\frac{1}{2\Delta b_i} [F_{y_i}(v_p - v_{p'}) + F_{y_e}(v_l - v_r)] \\ (G_{III})_j = -\frac{1}{2\Delta b_j} [F_{y_j}(v_q - v_{q'}) + F_{y_f}(v_m - v_{m'})] \quad (3) \\ (G_{III})_k = -\frac{1}{2\Delta b_k} [F_{y_k}(v_r - v_{r'}) + F_{y_s}(v_n - v_{n'})]$$

with

$$(G_{Total})_\gamma = (G_I + G_{II} + G_{III})|_\gamma, \text{ and} \quad (4)$$

γ =i, j and k indicate nodes at the debond front as shown in Figure 3(b).

The elements are assumed to have the same length, Δ , ahead of and behind the debond front (as shown in Figure 3). In Eqs. 1-3, the equivalent widths apportioned to the two corner debond-front nodes are b_i and b_k , and to the midside debond front node is b_j . These are

$$b_i = \frac{1}{6}[b_{J-1} + b_J], \\ b_j = \frac{2}{3}b_J, \quad (5) \\ b_k = \frac{1}{6}[b_J + b_{J+1}],$$

where b_{J-1} , b_J and b_{J+1} are the widths of element rows $J-1$, J and $J+1$, respectively, as shown in Figure 3(b). Note that this modeling strategy, which assumes no rotational constraints ahead of the debond front, is termed “Technique-B” in references 22,23. The strain energy release rates along the debond front of the mixed-mode skin-stiffenerdebond configurations are calculated using equations (1)-(5).

Modeling Stitches

The configurations have been analyzed with a geometrically nonlinear finite element analysis within the STAGS finite element code. Unlike the two-dimensional plane strain and three-dimensional solid models considered in references 27-31, the plate element-based modeling technique does not allow through-the-thickness modeling of details such as the stitches; nor does it allow nodal connections other than at the plate element reference surface. Thus, in the present technique, the stitches are not modeled as spar or beam elements, but rather as STAGS fastener elements.

The fastener elements are imposed as nonlinear springs offset by rigid links within the plate element model.^{15,16}

The fastener elements have both axial and shear stiffnesses, K_{axial} and K_{shear} and are schematically shown as springs in Figure 2. Only the fastener elements behind the debond front carry load since the upper and lower plate elements ahead of the debond front are coupled using constraint equations to have identical translational displacements. Stitches are considered in the model only along the debonded length of the lap joint, so the number of fastener elements in the model representing the stitches in the structure is dependent on the debond length. The fastener elements are evenly spaced along the debonded length of the model. The stitch location spacing presented in Table 1 coincides with plate element nodal locations.

Accurate compliance curves for both axial and shear behavior of the stitches were developed in reference³⁵ using flatwise tension and double lap shear tests (see Figure 4), respectively. These compliance curves represent the net behavior of the stitch due to stitch material nonlinearity and stitch debonding. The contribution due to the compliance of the stacks of carbon/epoxy has been accounted for and does not contribute to the values shown in the curves of Figure 4.³⁵

A piecewise linear representation of this data is used in the finite element model. The points used in the linearization of the compliance curves are also shown in Figure 4. Examination of the flatwise tensile test data revealed that the axial compliance of the stitches increases from approximately (1/77000) in./lb. initially to (1/2050) in./lb. near failure. Similar examination of the double lap shear test data showed that the shear compliance of the stitches increases from approximately (1/18200) in./lb. initially to (1/1600) in./lb. near failure. Since the axial and shear responses of the stitches shown in Figure 4 were determined independently using flatwise tension and double lap shear tests, their responses must be considered to be independent in the analysis as well. Also note that failure of the stitches occurs at a load of 58 lb. per stitch in tension and 38 lb. per stitch in shear. These stiffnesses and failure loads will be used for the characterizations in this paper.

Modeling the Contact Problem

Closure of the debond faces may occur once the debond is of sufficient length. In the finite element analysis, contact of the faces is allowed, while interpenetration of the faces is not. Interpenetration of the faces can be prevented either by adding gap elements (STAGS 810 PAD elements) to the model between the debond faces where interpenetration is likely to occur or by adding multipoint constraints along a known region of interpenetration to impose the requirement of identical z -direction (w) displacements among elements in contact. No constraint on the relative sliding displacements (u, v) is imposed using either technique. The multipoint

constraint-based procedure was used in the present analysis even though it requires that multiple analyses be executed to determine the actual contact length. This choice was made because of issues concerning the tolerances on overclosure allowed with the PAD elements.

Experimental Results

Since a limited amount of the material was available, only two replicates of each specimen configuration were tested. The failure loads of these specimens are presented in Table 2. The unstitched lap joint specimens catastrophically failed at the interface. The stitched lap joint specimens completely debonded at the interface while maintaining their load carrying capability. Final failure of these specimens was due to combined tensile and bending loads at the ends of the lap joint. Thus, the failure loads listed for the stitched specimen represent lower bounds.

Table 2: Test Specimen Failure Loads

Specimen	Unstitched (U) or Stitched (S)	Failure Load, lb.
Slap 1-1	U	4640
Slap 1-2	U	4407
Slap 1-1S	S	11820
Slap 1-2S	S	11630

Radiographic images were taken at periodic intervals during loading to determine the length of the debond at each applied load level. Figures 5 and 6 present the damage within representative lap joints of the unstitched and stitched configurations, respectively. For convenience in presentation, x -direction locations corresponding to $x=+L_2/2$ in Figure 2 are denoted the top of the lap joint, while x -direction locations corresponding to $x=-L_2/2$ are denoted the bottom of the lap joint.

Figure 5(a) shows the unstitched lap joint of length $L_2=3.69$ in. (see Figure 2) at zero load. As seen in the figure, there is no initial damage within the lap joint. Figure 5(b) shows a delamination of length, a , growing from the top of the lap. No debonds were observed growing near the bottom of the lap. This could be the result of a small asymmetry in the specimen or load frame and is likely due to the debond at the top of the lap initiating first and relieving the driving force at the bottom of the lap.

Recall that the equivalent laminate stacking sequence of each stack of material is (45/-45/0/90/0/-45/45)_{ns}. The primary debond shown in Figure 5(b) grew at the interface of 45° yarns. A split initiated in the 45° yarns and allowed a secondary debond to initiate and grow between the 45° and 0° yarns as shown in Figure 5(b).

Figure 5(c) shows the lap joint at a load of 4630 lb. Catastrophic failure due to unstable debond growth was observed at 4640 lb.

Figure 6 shows debond growth in the stitched lap joint. Figure 6(a) shows the stitched lap joint of length $L_2=3.69$ in. (see Figure 2) at zero load. As seen in the figure, only minor matrix cracks due to the curing stresses were observed at the top and bottom of the unloaded lap joint. Figure 6(b) shows the initial debond growth. In contrast to the unstitched material, debonds initiated at both ends of the stitched lap joint. Note that the load corresponding to these short debonds is much greater than the final failure load for the unstitched material indicating that the stitches tend to suppress the initiation of the debond. As with the unstitched material, there is some damage within the individual stacks of material during these early stages of debond growth.

Figure 6(c) through 6(f) show the specimen at various load levels and the corresponding debond evolution. There is some secondary damage evolution at the ends of the lap joint primarily due to bending stresses at the discontinuity of the lap. However, over most of its length, the debond is seen to grow along the well defined interface between the stacks. As seen in Figures 6(d) and 6(e) for longer debond lengths, the debond tends to grow somewhat faster along the free edges of the lap rather than near the center. Finally, Figure 6(f) shows a completely debonded lap joint that maintained a load of 11037 lb. At this applied load, all load was transferred through the stitches. Final failure occurred at 11820 lb. and was not due to stitch failure but was due to a tensile and bending stress failure at the ends of the lap. The value of 11820 lb. may be treated as a lower bound of load carrying capability for this specimen. Thus, the loads corresponding to a particular debond length are much larger for the stitched configuration than for the unstitched configuration and the average failure load of the stitched lap joints was 2.6 times the failure load of the unstitched lap joints.

Since the debond front shown in some of the radiographs was not straight, an average value was determined as the length of a straight debond of equivalent area. Figures 7(a) and 7(b) show average debond length as a function of applied load for the unstitched and stitched configurations, respectively. Curve fits were made using an equation of the form

$$a = a_0 + \frac{C}{P - P_0} \quad (6)$$

and are given in Figure 7. In equation 6, a is the crack length, P is the applied load, and a_0 , P_0 and C are constants from the curve fit. Due to the unstable nature

of the debond growth in the unstitched lap joint, only three debond measurements were obtained from the two unstitched specimens. In contrast, the progression of the debond in the stitched lap joint was stable and allowed several measurements to be taken as shown in Figure 7(b). The values were taken as separate measurements from both ends of the two stitched lap joint specimens.

Analytical Results

The experimentally determined average debond length vs. load curves presented in Figure 7 for the unstitched and stitched single lap joints were used as input parameters in the plate element-based finite element analysis. Since the single lap joint configuration has a finite width, it may exhibit mode I, mode II and mode III strain energy release rates. Also, although a straight debond front is employed to simplify the analyses, a variation in both strain energy release rate and stitch force may exist along the length (x -) and across the width (y -) of the lap joint. In the results that follow, quantities are given at a y location corresponding to an interior row of stitches near the centerline of the stitched configuration (stitch row 1) and at a y location corresponding to a row of stitches near the edge of the stitched configuration (stitch row 4). These y locations denoted as locations A and B correspond to stitch row 1 and stitch row 4 in Figure 2 and are located at $y=0.0625$ in. and $y=0.4375$ in., respectively, from the configuration centerline.

Figures 8 through 11 show the individual modes of the strain energy release rates and stitch forces for the two configurations at loads and debond lengths corresponding to the curves of Figure 7. For convenience and clarity, the individual modes of energy release rate and the stitch forces are plotted as functions of debond length. Because of antisymmetry about the x -direction midplane and symmetry about the y -direction midplane of the configuration, the curves presented in Figures 8 and 9 are valid for energy release rates and stitch forces in each of the four quadrants of the lap joint.

The values of strain energy release rate for loads corresponding to the debond lengths in Figure 7 are significantly greater than the G_{Ic} and G_{IIc} values determined for the 3501-6 resin used in the specimens.³⁸ Both the unstitched and stitched lap joint configurations are able to sustain these high G -values due to several energy absorbing phenomena. In the unstitched material, splitting of the 45° yarns and the formation and growth of a secondary debond between the 45° and 0° yarns seen in Figure 5(b) contribute to the apparent high value of strain energy release rate. In the stitched material, there is also some damage within the stacks of material as shown in Figures 6(b) and 6(c). This occurs over only a small portion of the debonded length of the

stitched lap joint. A full three-dimensional analysis may be required to account for the individual contributions of each of the damage mechanisms.³⁹ However, using the debond length and applied load from the experiment, the plate element-based analyses can predict the effective values of G as seen in Figure 8. These G -values can then be used as ranking parameters.

Figure 8(a) shows G -values plotted against debond length for the unstitched configuration with a debond at only one end of the single lap joint (corresponding to the configuration shown in Figure 5). Figure 8(a) shows two nonzero components of G at location A and three nonzero components of G at location B for the unstitched configuration. Mode I becomes increasingly significant at both locations as the debond grows. Mode II is the largest component of energy release rate and also increases with increasing debond length. Mode III has a value near zero (thus, not shown) at location A but increases near the edge.

Figures 8(b) and 9 show the G -values and stitch forces, respectively, plotted as functions of debond length for the stitched configuration with a debond at each end of the single lap joint (corresponding to the configuration shown in Figure 6). Because of symmetries and antisymmetries in the problem, the curves presented in Figures 8(b) and 9 are valid for energy release rates and stitch forces in each of the four quadrants of the lap joint. Figure 8(b) shows one nonzero component of G at location A and two nonzero components of G at location B for the stitched configuration. For all debond lengths and at both locations, the mode I component is near zero. As with the unstitched configuration, mode II is the dominant component and is seen to increase with debond length. Mode II is larger near the configuration centerline for short debonds but is larger near the configuration edge for longer debonds. As in the unstitched configuration, Mode III has a value near zero at location A but increases near the edge.

The three orthogonal components of stitch force at locations A and B are presented in Figures 9(a) through 9(f). Figure 9 shows how each of the stitches begins to carry load as the debond of length, a , passes its location in the model. Since the results were evaluated from the finite element model with increments of debond length of 0.125 in. ($2a/L_2=0.0678$), the force in the stitches for debond lengths corresponding to the interval between the stitch location and the next whole increment of debond length is not known and is represented by the dashed line.

Figures 9(a) and 9(b) show the axial force (F_{zz}) in stitch rows 1 and 4, respectively. In both rows, only the first two stitches (stitch columns 1 and 2) are loaded axially. Figures 9(c) and 9(d) show the longitudinal shear forces (F_{xz}) in stitch rows 1 and 4, respectively. In both rows,

all stitches are loaded and show increasing values of shear force as the debond grows. The values shown in Figures 9(c) and 9(d) for stitch rows 1 and 4 are almost identical. This is not unexpected as G_{II} values at locations A and B are similar. Finally, Figures 9(e) and 9(f) show the transverse shear forces (F_{yz}) in stitch rows 1 and 4, respectively. The transverse forces in row 1 are very small for all stitches at all debond lengths corresponding to near zero values of G_{III} at location A . However, the transverse forces in row 4 approach about thirty percent of the shear failure load of the stitches corresponding to the larger values of G_{III} at location B . The shape of the debond in Figure 6(d) is a result of larger values of G_{II} and G_{III} at the configuration edge than at the centerline. This corresponds to the increased transverse shear force in the stitches near the free edge.

Concluding Remarks

The effect of stitches on the failure of single lap joint configuration was studied. An experimental program was conducted to determine the loads necessary to grow the debond through complete debonding of the specimens. Modeling was performed using a method that uses the virtual crack closure technique to calculate the strain energy release rates, plate elements with an offset reference surface to model the configuration, nonlinear fastener elements to model the stitches and multipoint constraints to model the contact problem.

The stitches were shown to delay the initiation of the debond and provide load transfer beyond the load necessary to completely debond the lap joint. Radiographs of the unstitched lap joint indicated that a debond initiated and grew from only one end of the lap joint. This could be the result of a small asymmetry in the specimen or load frame. Radiographs of the stitched lap joint indicated that the debond initiated at a higher load than in the unstitched lap joint and grew from both ends of the lap joint with neither debond dominating the other. For the configurations considered, the failure load of the stitched lap joints was about two and a half times the failure load of the unstitched lap joints.

The experimentally determined debond length vs. applied load was used as an input parameter in the finite element analysis. The plate element-based finite element analysis is suited for configurations that would normally lend themselves to being modeled with plate elements, that is, configurations wherein shear deformable plate assumptions are valid. In models of the stitched configuration, the stitches were modeled as discrete nonlinear fastener elements with their compliance determined by experiment. Both axial and shear behavior of the stitches were considered, however, the two compliances and failure loads were assumed to be independent. The contact problem was modeled using multipoint constraints rather than gap elements

because the no penetration condition could be imposed exactly with the multipoint constraints whereas the gap elements enforce no penetration to a small but finite tolerance that is significant in this analysis.

Models of the unstitched configuration showed that the nonzero components of strain energy release rate vary nearly linearly with debond length. All three modes increase with increasing debond length at both near the configuration centerline and near the configuration free edge. Mode II is the largest of the three components, while mode III is the smallest.

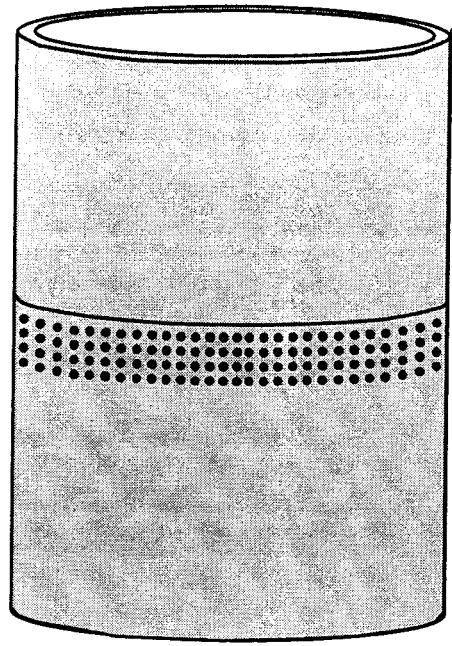
Models of the stitched configuration showed that only one nonzero component of G exists near the centerline while only two nonzero components exist near the free edge. The stitches reduce G_I to near zero values for all debond lengths. However, the stitches are much less effective in reducing G_{II} as it is the dominant component and is seen to increase over the entire range of debond lengths considered. Mode II becomes larger near the free edge than near the centerline with increasing load. Mode III is significant only near the free edge. The longer debond at the free edges of the specimen at higher loads may be attributed to these two phenomena.

Only the first two rows of stitches carry axial load over all debond lengths considered. Longitudinal shear force is transferred by all rows of stitches in the debonded region and increases with increasing debond length. The longitudinal shear force is nearly independent of the proximity of the stitch to the free edge. In contrast, transverse shear force in the stitches near the free edge is much larger than in the stitches near the centerline.

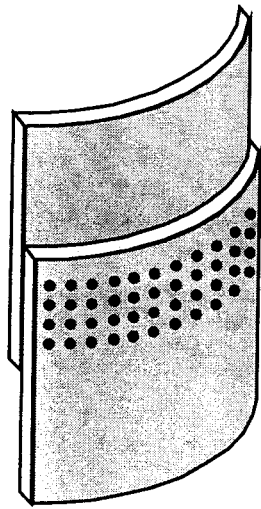
References

1. Davis, J.G., Shuart, M.J. and Bowles, D.E., Eds., *Fifth NASA/DoD Advanced Composites Technology Conference*, NASA CP 3294, May 1995.
2. Wang, J.T., Jegley, D.C., Bush, H.G. and Hinrichs, S.C., "Correlation of Structural Analysis and Test Results for the McDonnell Douglas Stitched/RFI All-Composite Wing Stub Box," *NASA TM-110267*, 1996.
3. Smith, P.A. and Pascoe, K.J., "The Effect of Stacking Sequence on the Bearing Strengths of Quasi-Isotropic Composite Laminates," *Composite Structures*, Vol. 6, 1986, pp. 1-20.
4. Crews, Jr., J.H. and Naik, R.A., "Combined Bearing and Bypass Loading on a Graphite/Epoxy Laminate," *Composite Structures*, Vol. 6, 1986, pp. 21-40.
5. Smith, P.A., Pascoe, K.J., Polak, C. and Stroud, D.O., "The Behavior of Single-Lap Bolted Joints in CFRP Laminates," *Composite Structures*, Vol. 6, 1996, pp. 41-55.
6. Brookstein, D.S., "Joining Methods for Advanced Braided Composites," *Composite Structures*, Vol. 6, 1996, pp. 87-94.
7. Brinson, H.F. and Grant, J.W., "Mechanical Properties for Durability Predictions of FRP Bonded Joint," *Composite Structures*, Vol. 6, 1986, pp. 107-121.
8. Griffin, O.H., et. al., "Analysis of Multifastener Composite Joints," *Journal of Spacecraft and Rockets*, Vol. 31, No. 2, March-April 1994, pp. 278-284.
9. Hart-Smith, L.J., "Adhesive Bond Stresses and Strains at Discontinuities and Cracks in Bonded Structures," *Journal of Engineering Materials and Technology*, Vol. 100, January 1978, pp. 16-24.
10. Keer, L.M., "Stress Analysis for Bonded Layers," *Journal of Applied Mechanics*, September 1974, pp. 679-683.
11. Cohen, D., et. al., "Failure Criterion for Thick Multifastener Graphite-Epoxy Composite Joints," *Journal of Composites Technology and Research*, Vol. 17, No. 3, July 1995, pp. 237-248.
12. Shyprykevich, P., "Characterization of Bolted Joint Behavior: MIL-HDBK-17 Accomplishments at Standardization," *Journal of Composites Technology and Research*, Vol. 17, No. 3, July 1995, pp. 260-270.
13. *Military Handbook 17*, Volume 3, Materials Usage, Chapter 5, Structural Behavior of Joints.
14. Dow, M.B. and Dexter, H.B., "Development of Stitched, Braided and Woven Composite Structures in the ACT Program and at Langley Research Center," *NASA TP-97-206234*, November 1997.
15. Brogan, F.A., Rankin, C.C., Cabiness, H.D. and Loden, W.A., *STAGS User Manual*, Lockheed Martin Missiles and Space Co., July 1996.
16. Young, R.D., Rankin, C.C., Starnes, J. and Britt, V., *Introduction to STAGS*, Lecture Notes from a Workshop at NASA Langley Research Center, Hampton, VA, March 8-9, 1995.
17. O'Brien, T.K., "Characterization of delamination onset and growth in a composite laminate," *Damage in Composite Materials, ASTM STP 775*, 1982, pp. 140-167.
18. Wang, A.S.D. and Crossman, F.W., "Initiation and growth of transverse cracks and edge delamination in composite laminates, Part 1: An energy method," *Journal of Composite Materials*, Vol. 14, 1980, pp. 71-87.
19. Whitcomb, J.D., "Instability-related delamination growth of embedded and edge delaminations," *NASA TM 100655*, 1988.
20. Wang, J.T., Raju, I.S., and Sleight, D.W., "Composite Skin Stiffener Debond Analyses Using Fracture Mechanics Approach with Shell Elements," *Composites Engineering*, Vol. 5, No. 2, 1995, pp. 277-296.
21. Raju, I.S., Sistla, R., Krishnamurthy, T., "Fracture Mechanics Analyses for Skin-Stiffener Debonding," *Engineering Fracture Mechanics*, Vol. 54, No. 3, 1996, pp. 371-385.
22. Wang, J.T., Raju, I.S., Davila, C.G. and Sleight, D.W., "Computation of Strain Energy Release Rates for

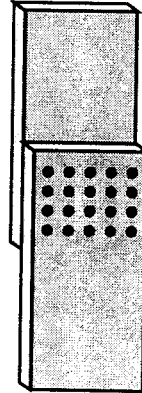
- Skin-Stiffener Debonds Modeled with Plate Elements," *34th AIAA/ASME/ASCE/AHS Structures, Structural Dynamics and Materials Conference*, AIAA Paper 93-1501-CP, 1993, pp. 1680-1692.
23. Wang, J.T. and Raju, I.S., "Strain Energy Release Rate Formulae for Skin-Stiffener Debond Modeled with Plate Elements," *Engineering Fracture Mechanics*, Vol. 54, No. 2, 1996, pp. 211-228.
24. Glaessgen, E.H., Riddell, W.T. and Raju, I.S., "Effect of Shear Deformation and Continuity on Delamination Strain Energy Release Rate," *39th AIAA/ASME/ASCE/AHS Structures, Structural Dynamics and Materials Conference*, AIAA Paper 98-2023-CP, 1998.
25. Glaessgen, E.H., Raju, I.S. and Poe, Jr., C.C., "Fracture Mechanics Analysis of Stitched Stiffener-Skin Debonding," *39th AIAA/ASME/ASCE/AHS Structures, Structural Dynamics and Materials Conference*, AIAA Paper 98-2022-CP, 1998.
26. Glaessgen, E.H., Raju, I.S. and Poe, Jr., C.C., "Plate Element-Based Models for Mixed-Mode Debonding of Stitched Stiffened Panels," *STP 1360, Fatigue and Fracture Mechanics: 30th Volume*, ASTM, 1998, in press.
27. Mignery, L.A., Tan, T.M., and Sun, C.T., "The Use of Stitching to Suppress Delamination in Laminated Composites," *ASTM STP 876*, 1985, pp. 371-385.
28. Chen, V.L., Wu, X.X., and Sun, C.T., "Effective Fracture Toughness in Stitched Laminates," *Proceedings of the Eighth Technical Conference of the ASC*, 1994, pp. 453-462.
29. Sharma, S.K. and Sankar, B.V., "Effects of Through-the-Thickness Stitching on Impact and Interlaminar Fracture Properties of Textile Graphite/Epoxy Laminates," *NASA CR195042*, 1995.
30. Sankar, B.V. and Sonik, V., "Modeling End-Notched Flexure Tests of Stitched Laminates," *Proceedings of the American Society for Composites*, ASC, 1995, pp. 172-181.
31. Byun, J.-H., Gillespie, Jr., J.W. and Chou, T.-W., "Mode I Delamination of a Three-Dimensional Fabric Composite," *Journal of Composite Materials*, Vol. 24, May 1990, pp. 497-518.
32. Flanagan, G. and Furrow, K., "Parametric Studies of Stitching Effectiveness for Preventing Substructure Disbond," *Mechanics of Textile Composites Conference, NASA CP 3311*, October 1995, pp. 539-554.
33. Tsai, G.C., "Global/Local Stress Analysis of Stitched Composite Laminates," *Proceedings of the 23rd International SAMPE Technical Conference*, SAMPE, 1991, pp. 297-305.
34. Lee, C. and Liu, D., "Tensile Strength of Stitching Joint in Woven Glass Fabrics," *Journal of Engineering Materials and Technology*, Vol. 112, April 1990, pp. 125-130.
35. Adams, D.O., "Stitch Compliance in Delaminated Composites," *29th SAMPE Technical Conference*, Orlando, FL, October 28-31, 1997.
36. Rybicki, E.F. and Kanninen, M.F., "A Finite Element Calculation of Stress Intensity Factors by a Modified Crack Closure Integral," *Engineering Fracture Mechanics*, Vol. 9, 1977, pp. 931-938.
37. Raju, I.S., "Calculation of Strain-Energy Release Rates with Higher Order and Singular Finite Elements," *Engineering Fracture Mechanics*, Vol. 28, No. 3, 1987, pp. 251-274.
38. Reeder, J.R., "A Bilinear Failure Criterion for Mixed-Mode Delamination," *ASTM STP 1206*, E.T. Camponeschi, Jr., Ed., ASTM, Philadelphia, PA, 1993, pp. 303-322.
39. Cvitkovich, M.K., Krueger, R., O'Brien, T.K. and Minguet, P.J., "Debonding in Composite Skin/Stringer Configurations Under Multi-Axial Loading," *Proceedings of the 13th Annual Technical Conference on Composite Materials*, American Society for Composites, Baltimore, ISBN 0-9667220-0-0 (CD-ROM), 1998, pp. 1014-1048.



(a) Cylindrical section with stitched lap joint



(b) Detail of stitched lap joint



(c) Simplified stitched lap joint configuration

Figure 1. Stitched joint configurations.

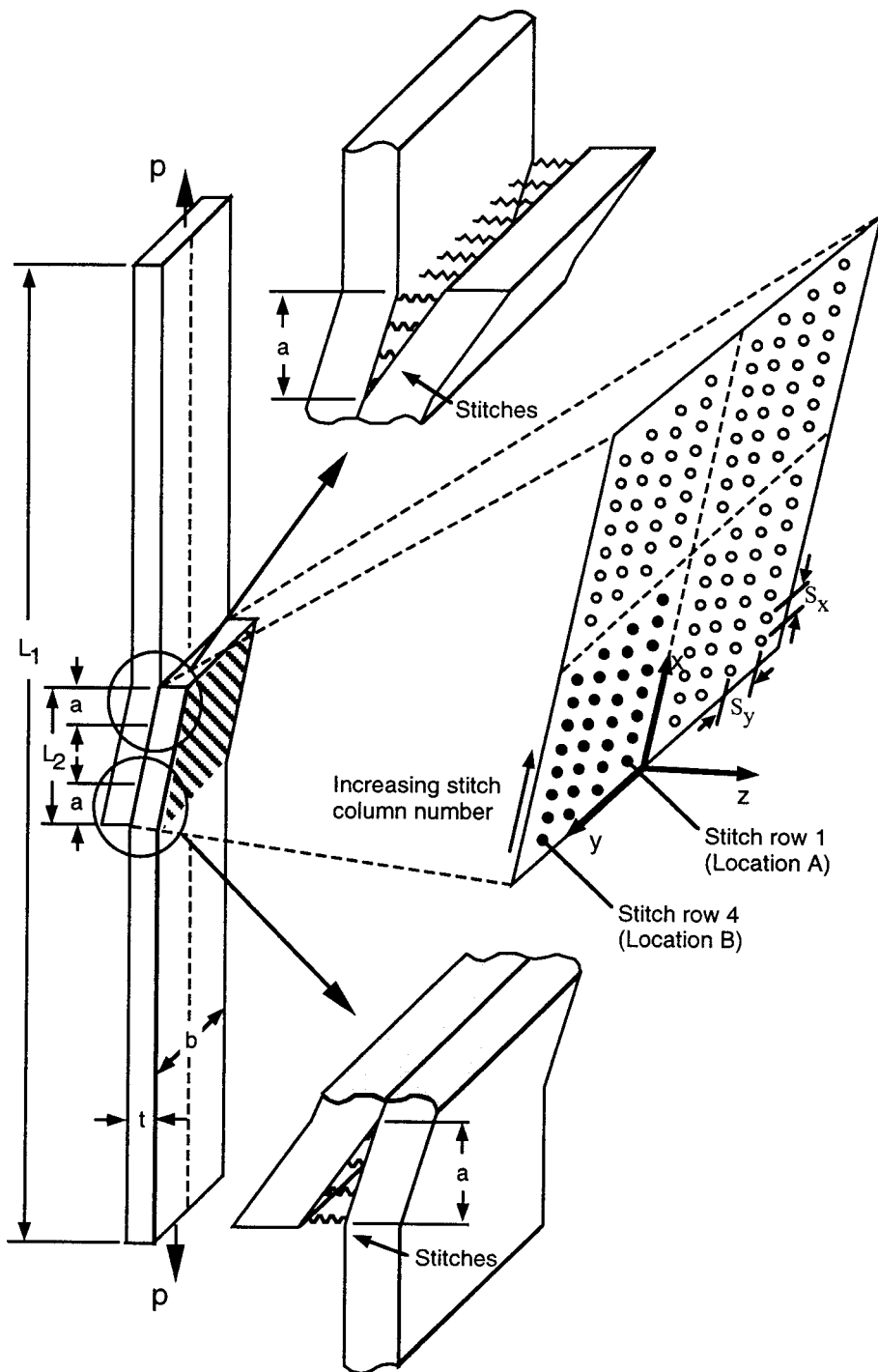
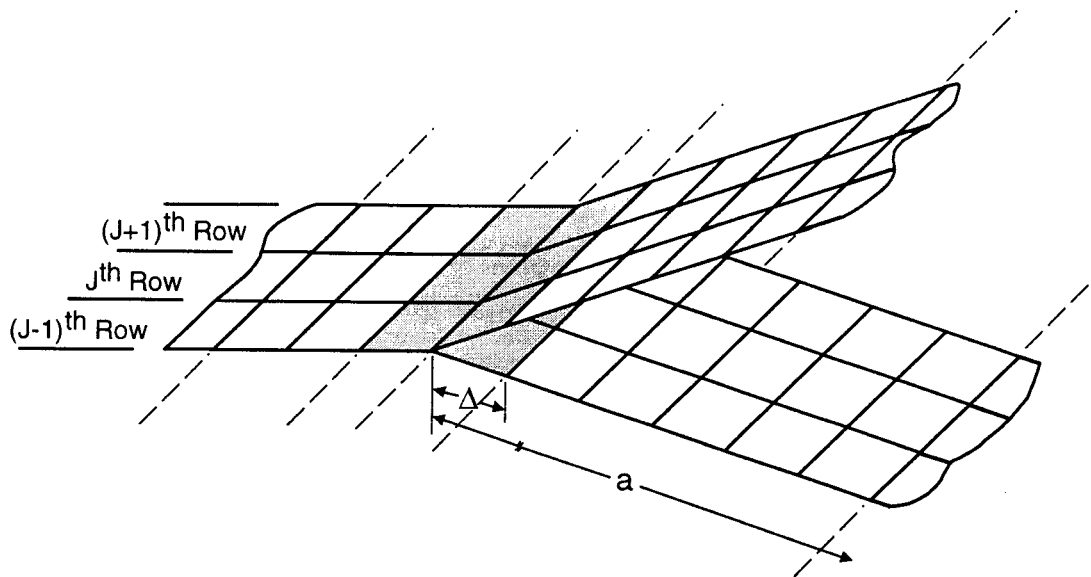
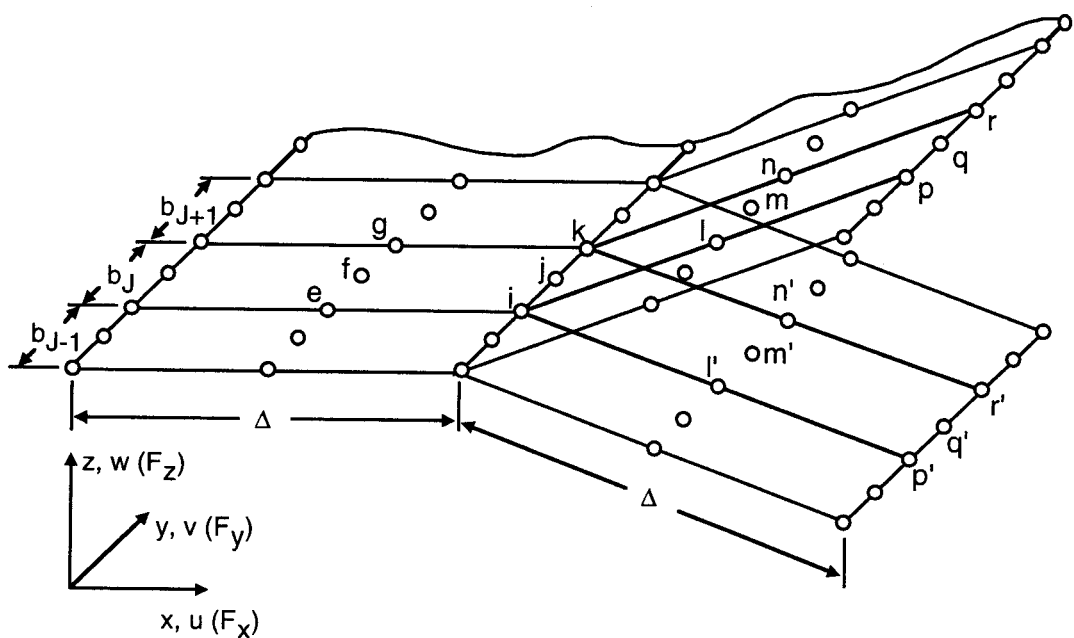


Figure 2. Stitched joint configurations.

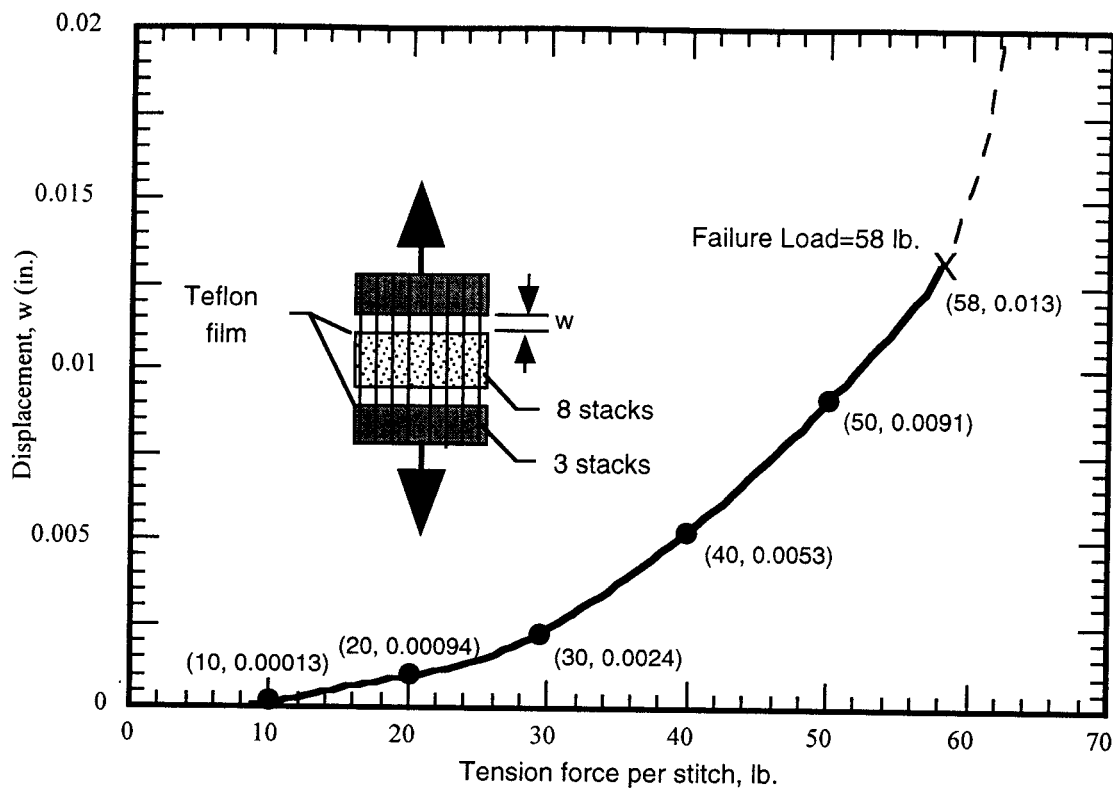


(a) Plate element modeling near the debond front

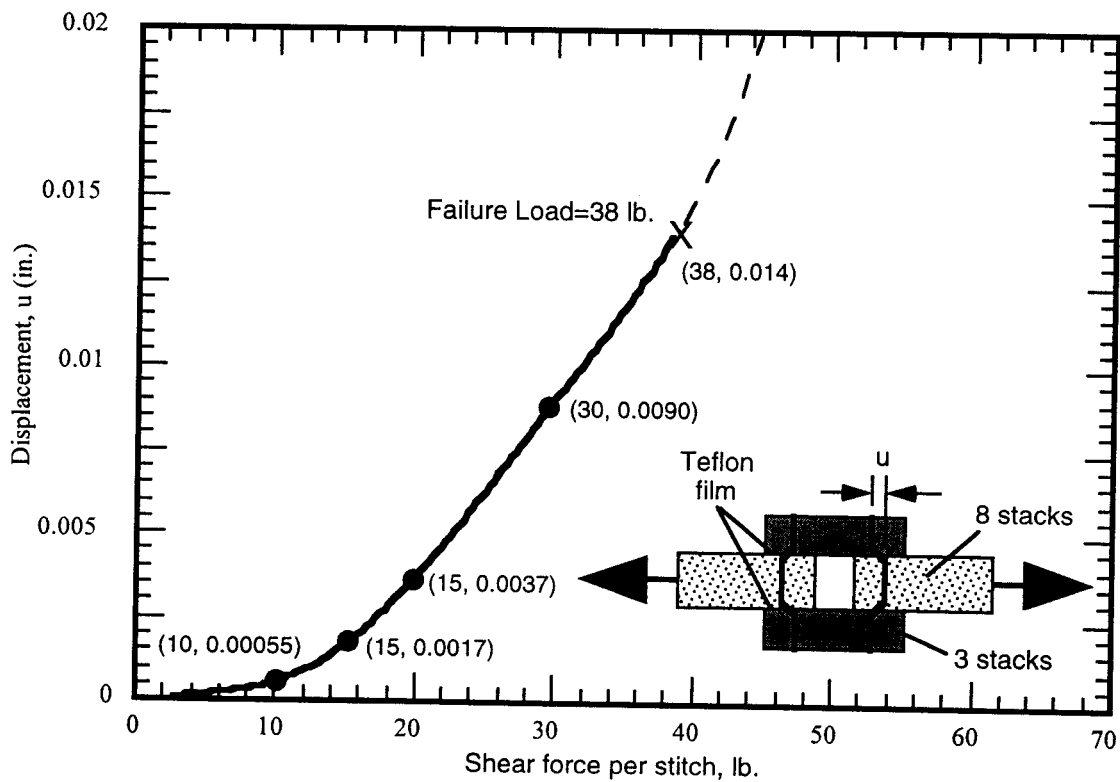


(b) Details of the model near the debond front

Figure 3. Lap joint configuration modeled using 9-node plate elements.

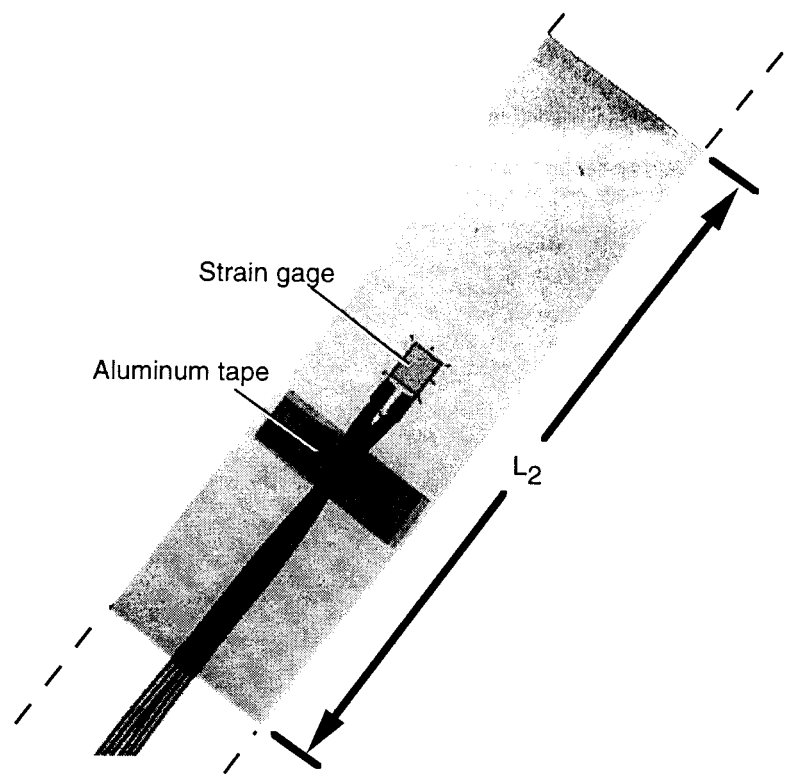


(a) Compliance of stitches in tension

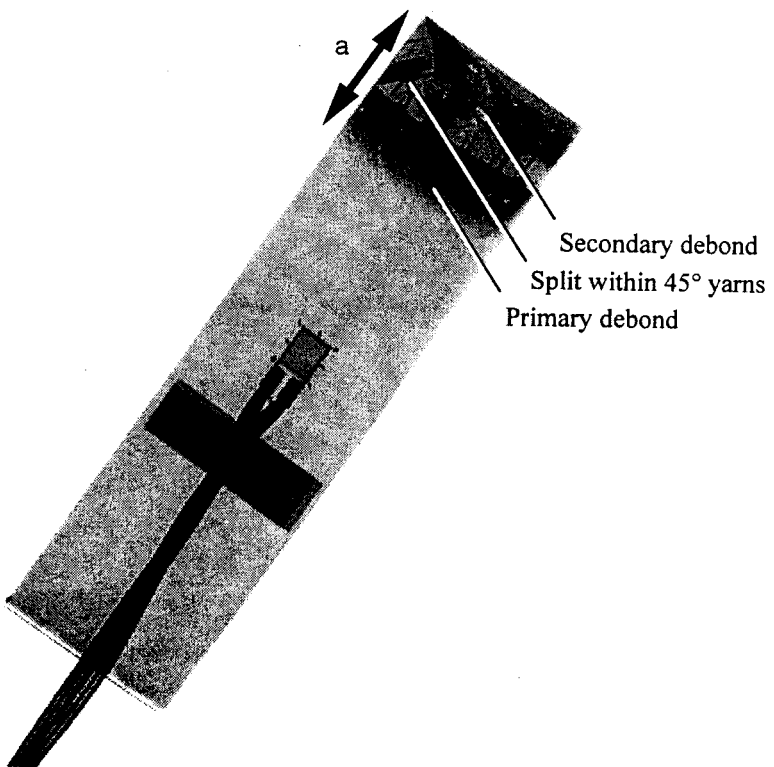


(b) Compliance of stitches in shear

Figure 4. Stitch compliance (experimental results taken from reference 33).

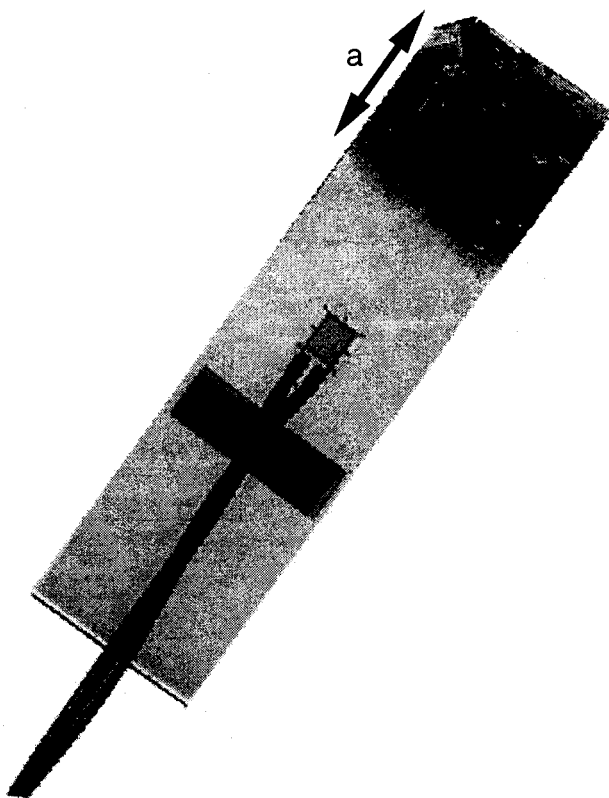


(a) Specimen at zero load (Debond length, $a=0/32$ in.)



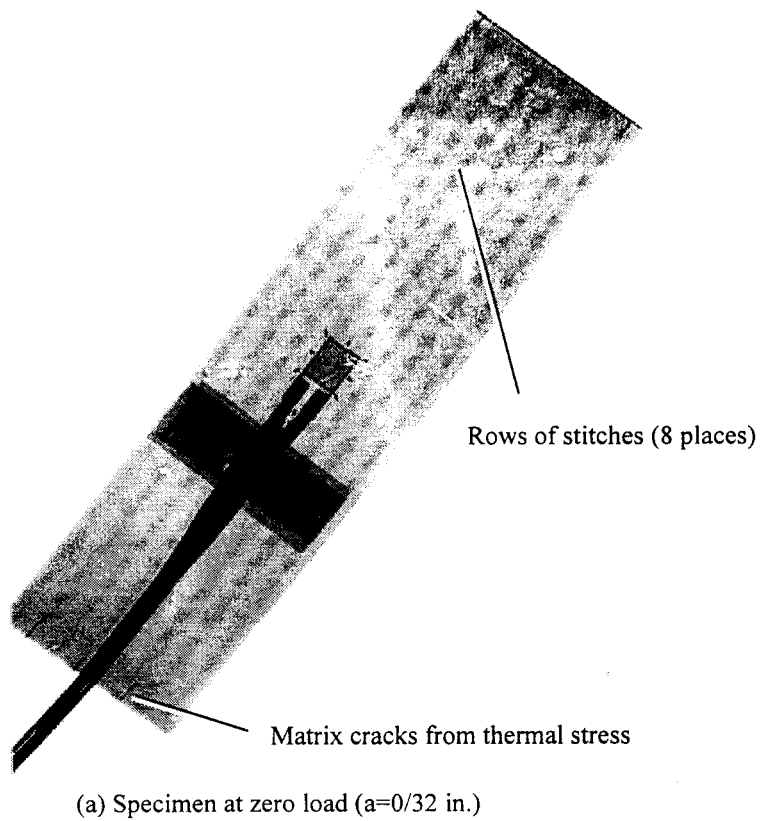
(b) Specimen at $P=4300$ lb. ($a=25/32$ in.)

Figure 5. Radiographs showing debond in unstitched lap joint.

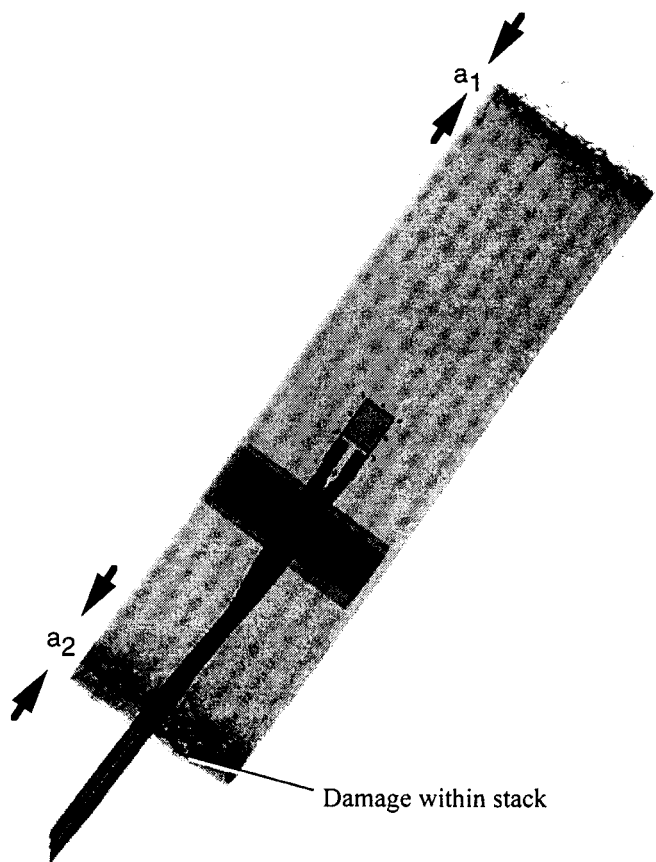


(c) Debond at P=4630 lb. (a=33/32 in.)

Figure 5. Radiographs showing debond in unstitched lap joint.

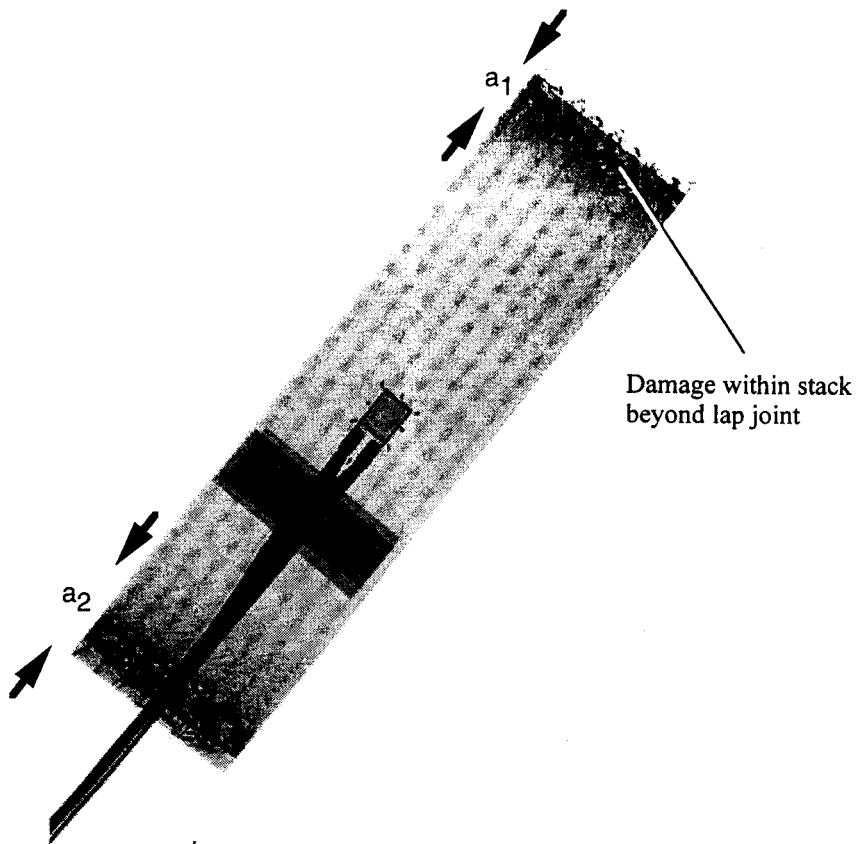


(a) Specimen at zero load ($a=0/32$ in.)

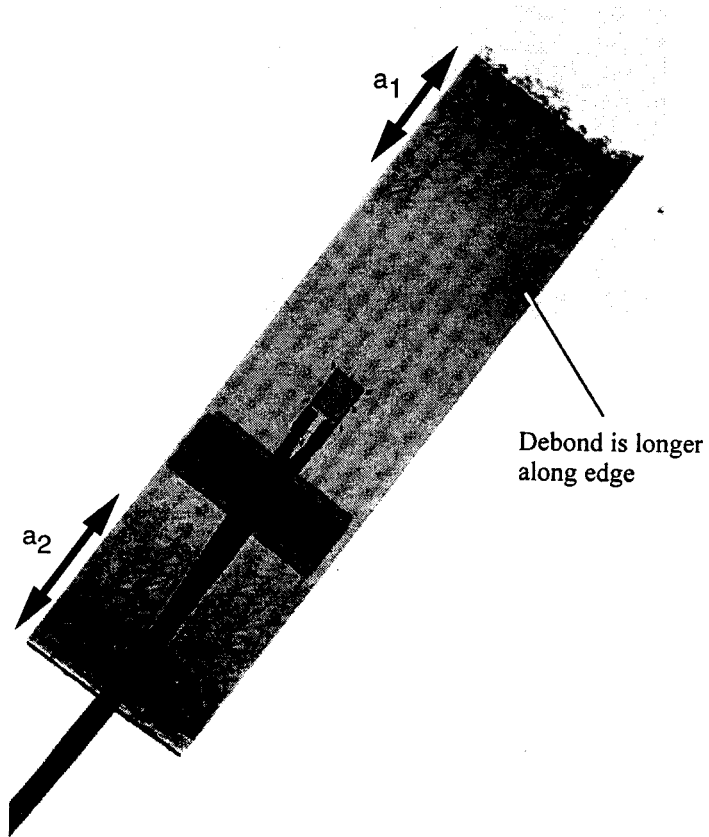


(b) Specimen at $P=5730$ lb. ($a_1=5/32$ in., $a_2=9/32$ in.)

Figure 6. Radiographs showing debond in stitched lap joint.

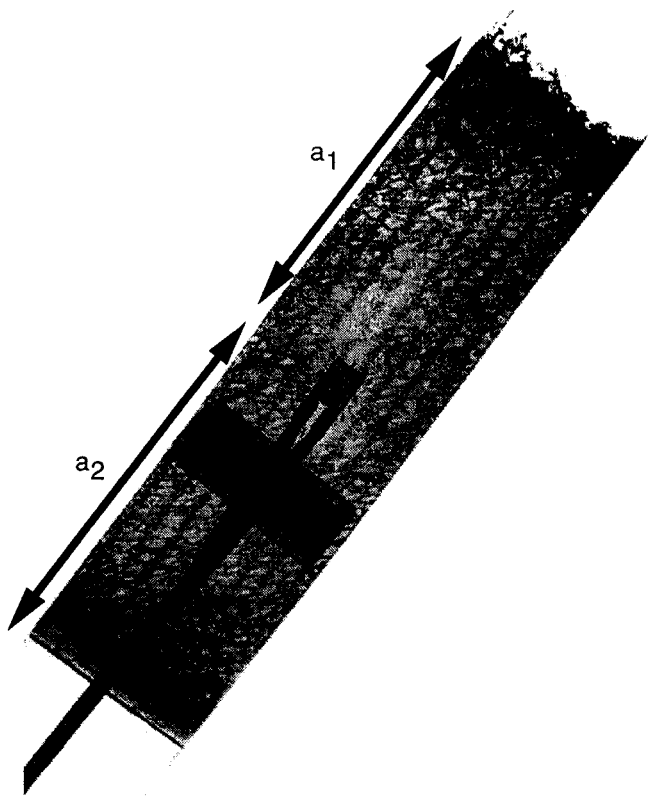


(c) Specimen at $P=7757$ lb. ($a_1=12/32$ in., $a_2=21/32$ in.)

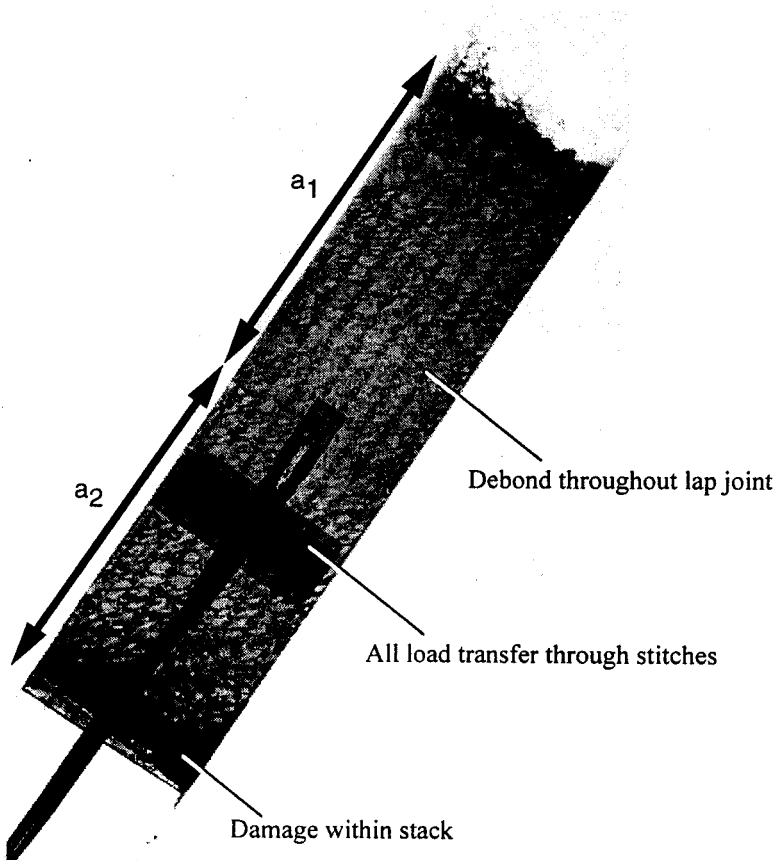


(d) Specimen at $P=9400$ lb. ($a_1=32/32$ in., $a_2=26/32$ in.)

Figure 6. Radiographs showing debond in stitched lap joint.

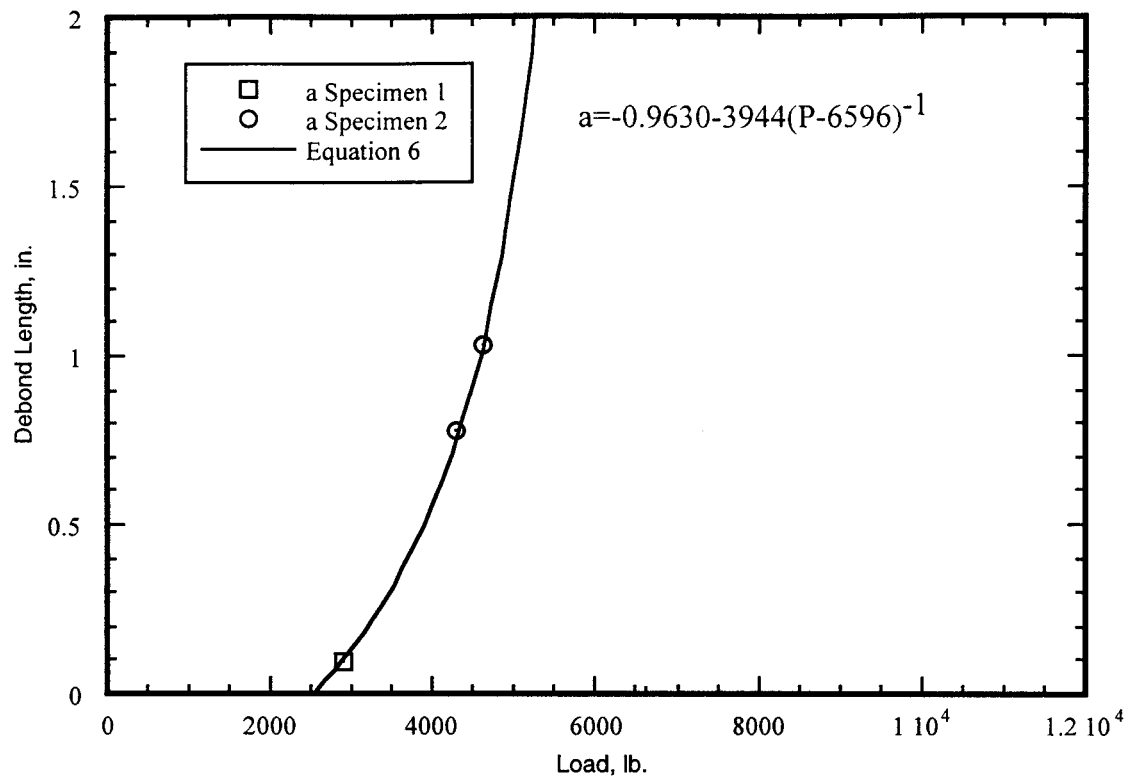


(e) Specimen at $P=10527$ lb. ($a_1=57/32$ in., $a_2=59/32$ in.)

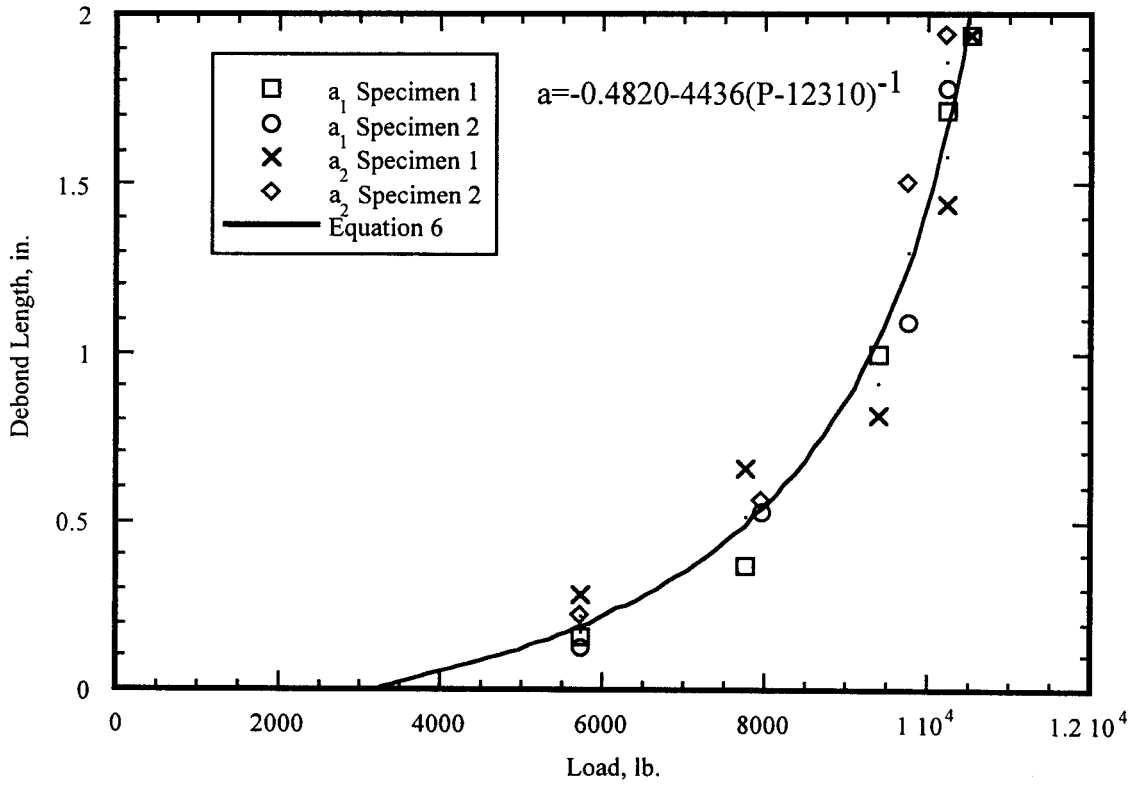


(f) Specimen at $P=11037$ lb. ($a_1=59/32$ in., $a_2=59/32$ in.)

Figure 6. Radiographs showing debond in stitched lap joint.

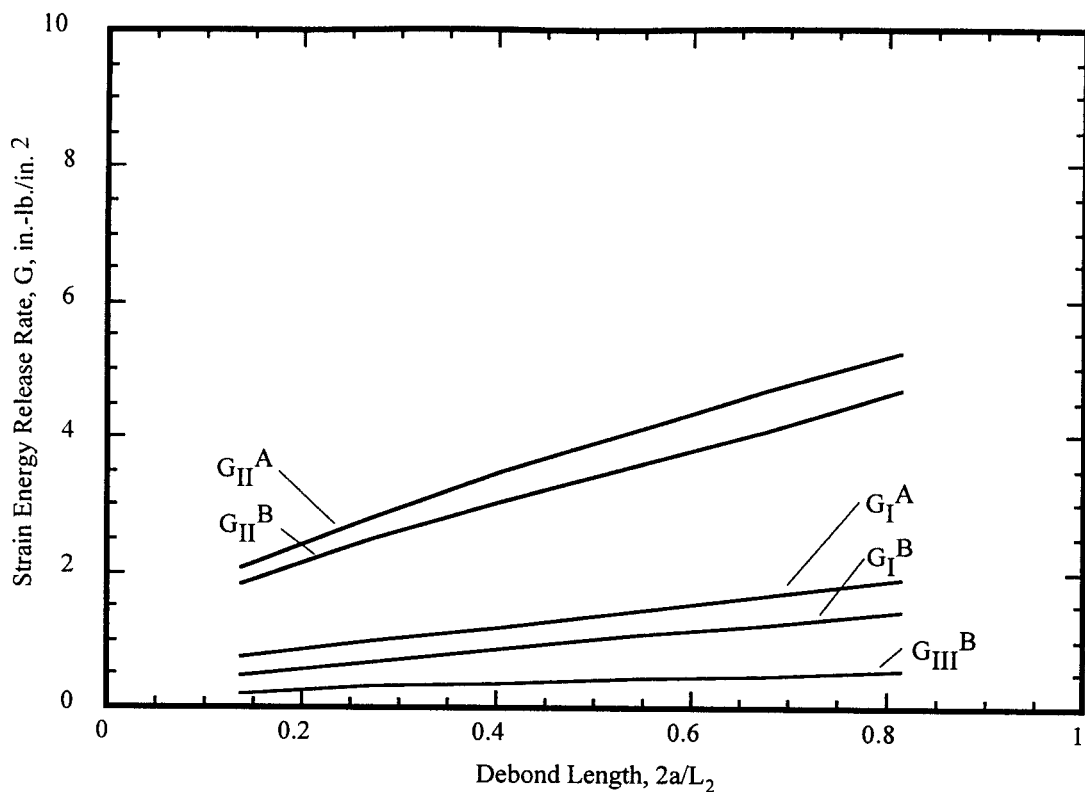


(a) Unstitched configurations

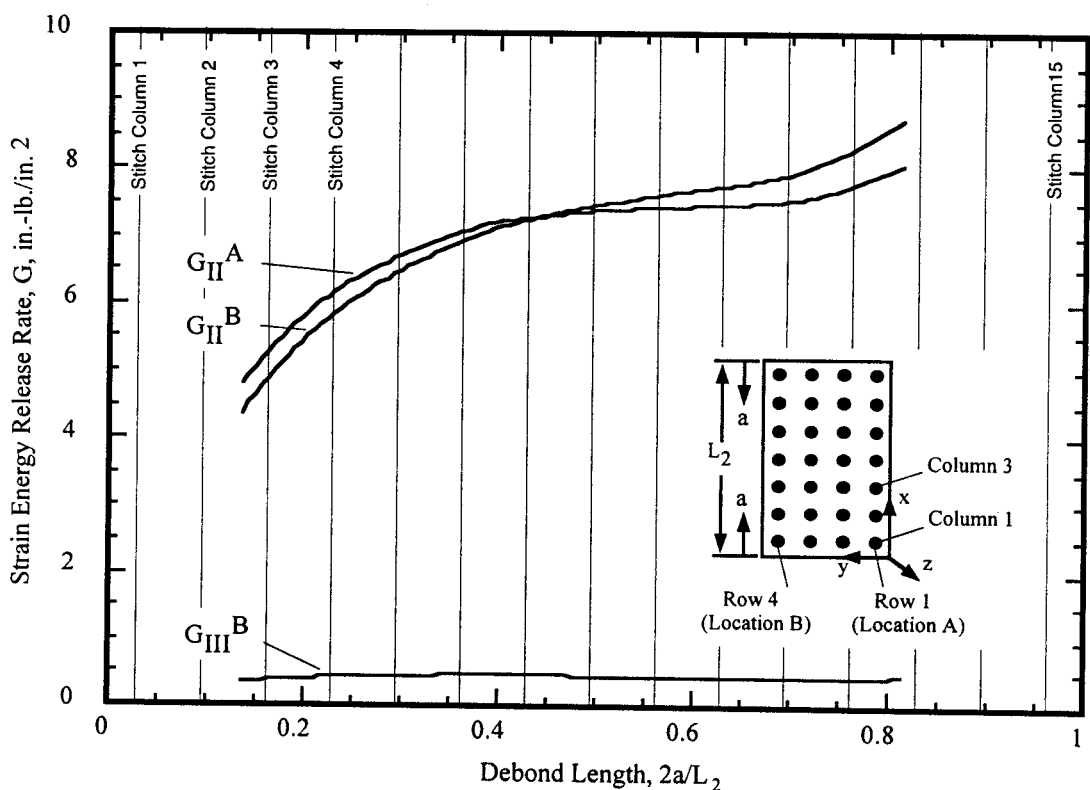


(b) Stitched configurations

Figure 7. Average debond length vs. applied load.

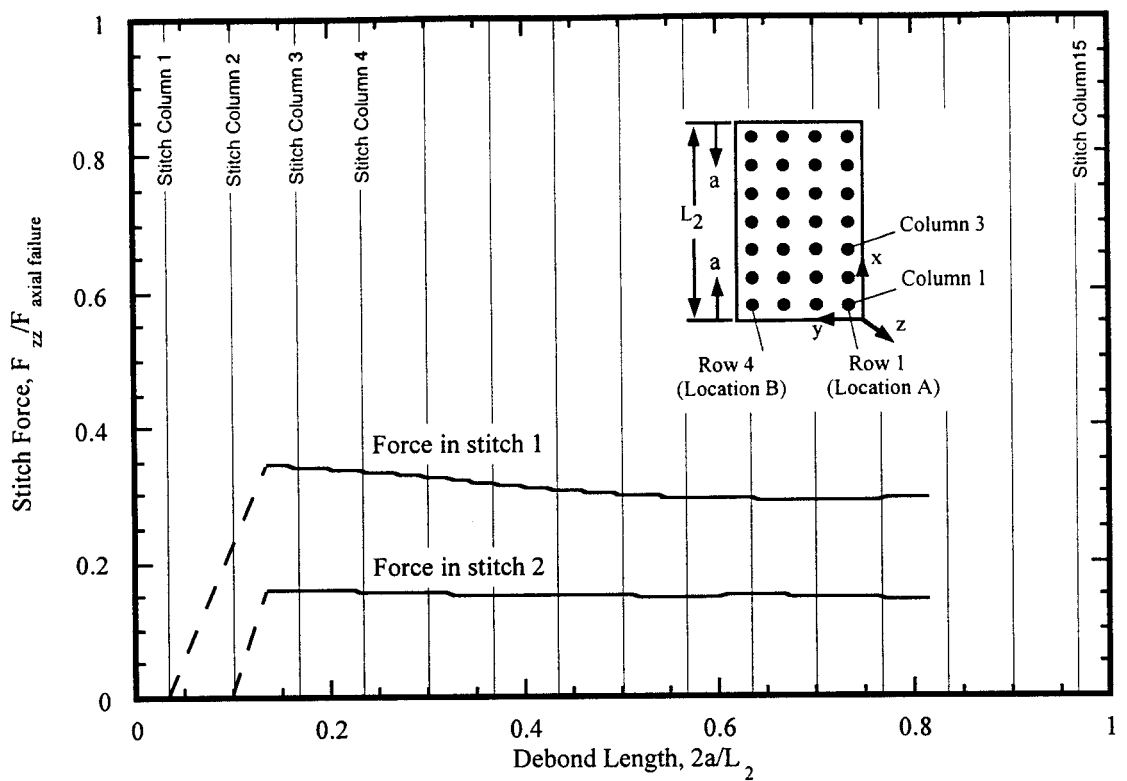


(a) Strain energy release rate in unstitched lap joint

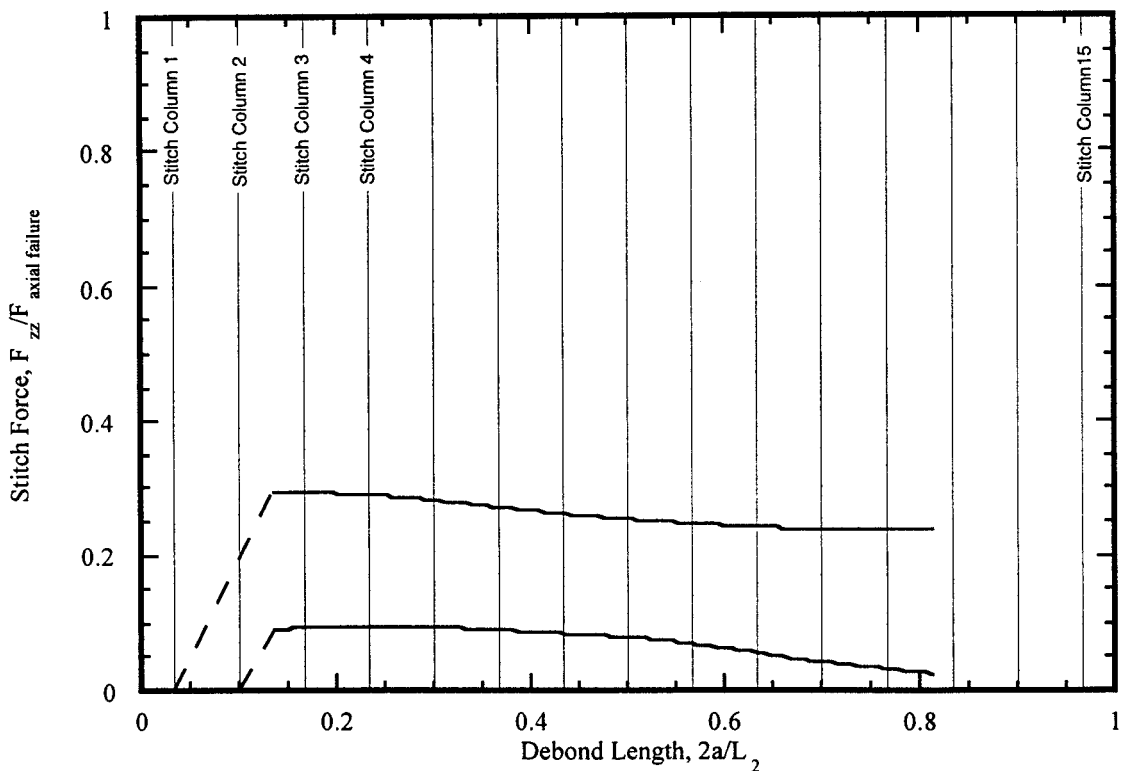


(b) Strain energy release rate in stitched lap joint

Figure 8. Strain energy release rates.

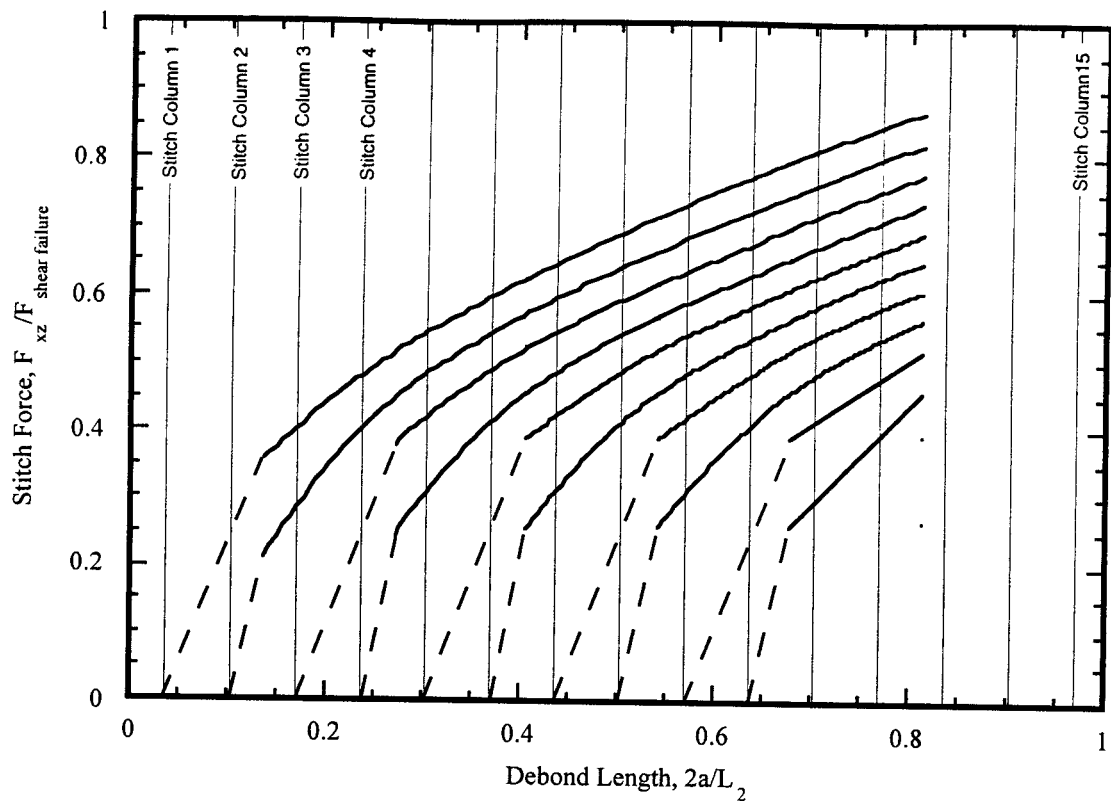


(a) Axial forces in stitch row 1

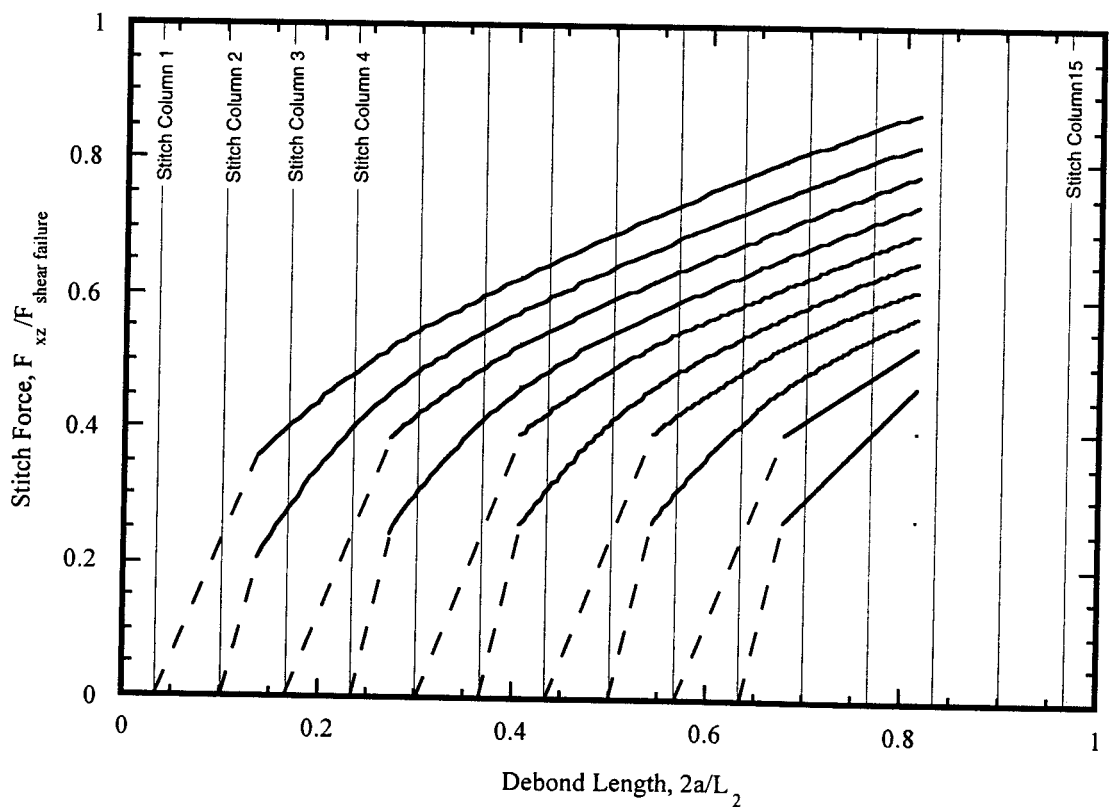


(b) Axial forces in stitch row 4

Figure 9. Stitch forces.

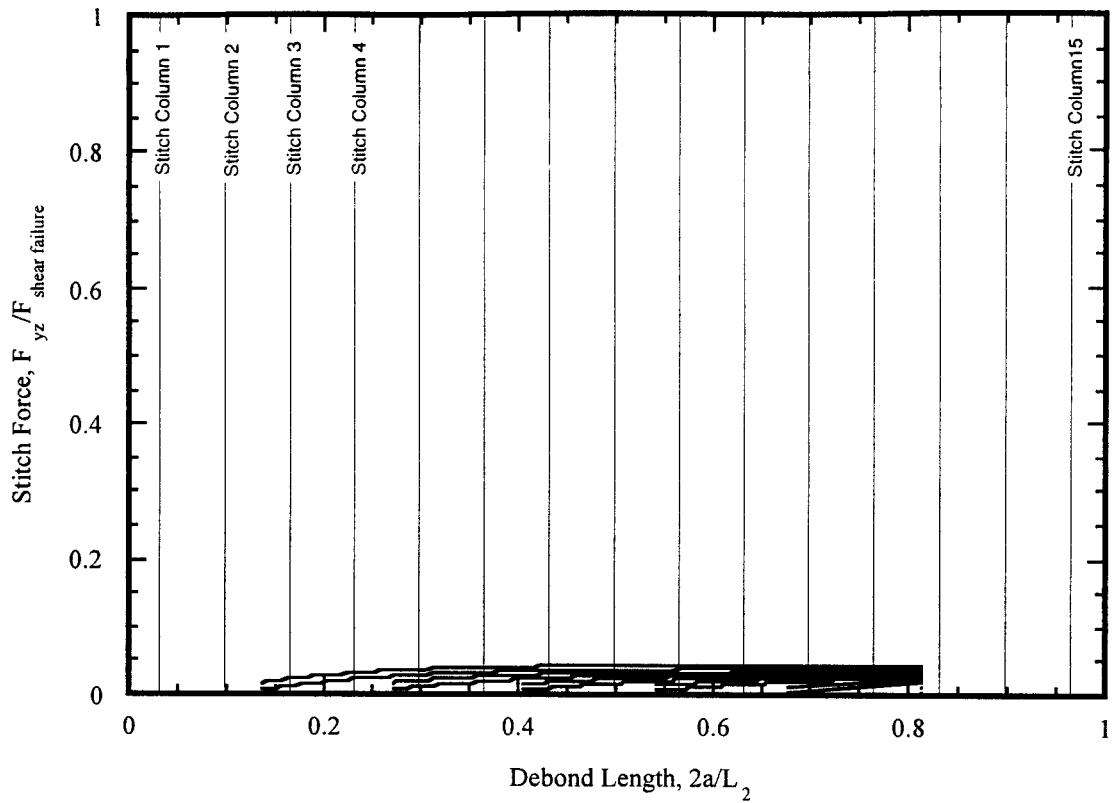


(c) Longitudinal shear forces in stitch row 1

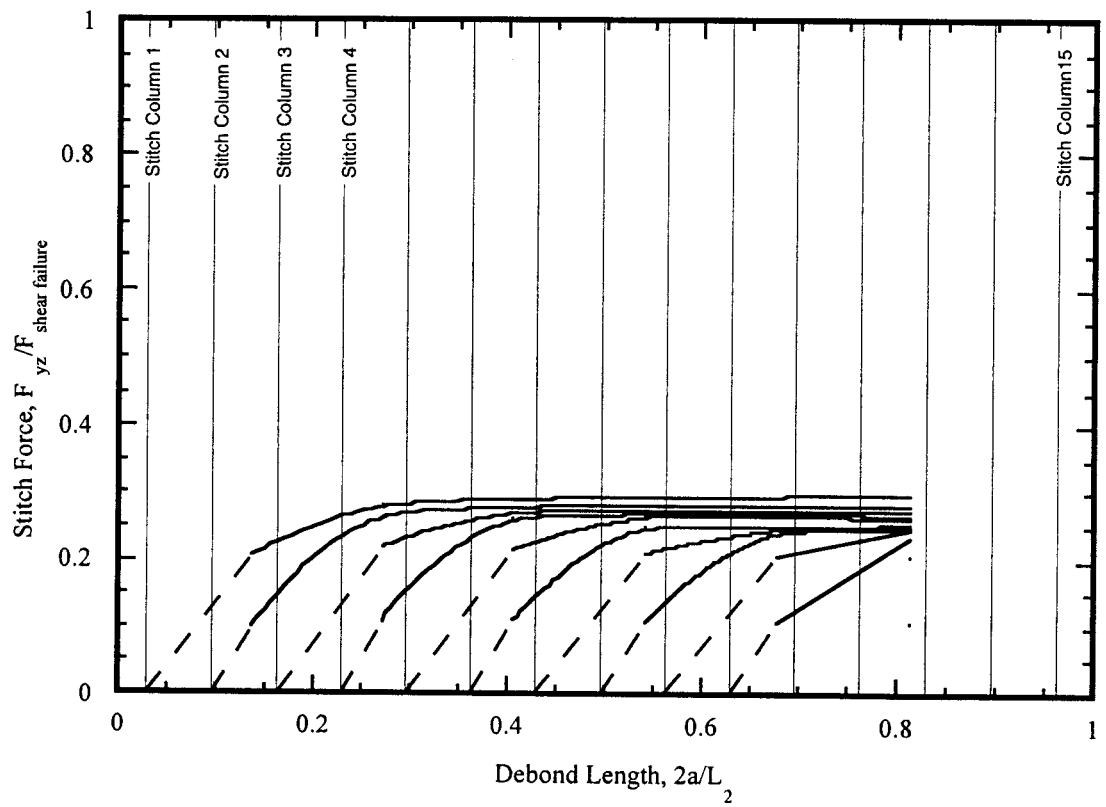


(d) Longitudinal shear forces in stitch row 4

Figure 9. Stitch forces.



(e) Transverse shear forces in stitch row 1



(f) Transverse shear forces in stitch row 4

Figure 9. Stitch forces.